Carbon nanotube reinforced nanocomposites for energy conversion and storage

Oluwafunmilola Ola [a,*], Qijian Niu [b], Yu Chen [a], Yongde Xia [a], Yanqiu Zhu [a]

[a] College of Engineering, Mathematics and Physical Sciences, University of Exeter, EX4 4QF, UK
[b] School of Agricultural Equipment Engineering, Jiangsu University, Zhenjiang, Jiangsu, 212013, China

HIGHLIGHTS

- CNT-reinforced nanocomposites were prepared from polymeric templates.
- Optimal nanocomposite exhibits excellent HER activity and specific capacitance.
- CNT-reinforced nanocomposite demonstrates high stability.

GRAPHICAL ABSTRACT
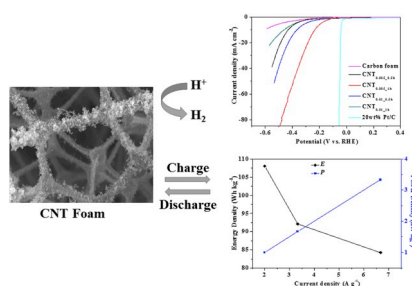
ABSTRACT

CNT-reinforced foams comprised of three-dimensional (3D) interconnected macropores with uniform mesoporous walls were developed as multifunctional nanocomposites and tested for electrochemical energy conversion and storage. Multi-walled CNTs grown on the wall surface of the interconnected scaffold structure of carbon foams were found to improve the surface area and electrochemical properties of the nanocomposites. The lightweight CNT-reinforced nanocomposites not only exhibit high structural flexibility, but also possess enhanced electrocatalytic performance for HER at current density of $10\,mA\,cm^{-2}$ with overpotentials of 240 mV. In addition, these nanocomposites can be used as flexible, electric double layer capacitor electrodes, and have achieved a specific capacitance of $776\,F\,g^{-1}$, with excellent durability and stability after 1000 cycles.

1. Introduction

Due to the unique combination of structural and physicochemical properties, polymer matrix nanocomposites have been extensively studied for applications ranging from automotive, biosensors to energy storage [1]. These materials exhibit remarkable improvement in mechanical stability, flexibility, electrical and thermal properties over their plain matrixes, and provide opportunities to specifically tune the morphology, particle size and pore structure of final nanocomposites towards a diverse application. The lightweight and good load bearing capacity of most polymeric substrates especially foams make them ideal candidates for thermal insulation, shock or acoustic energy damping among others [2]. However, most polymeric substrates have limited applicability for energy related applications due to low thermal/-electrical conductivity and flexibility linked to their amorphous polymer chain [3]. The capability of polymeric matrixes can however be

enhanced by organic and/or inorganic nanofillers during their processing [2]. The enhancement effect to the matrix is linked to the physicochemical properties of the nanofiller, its optimal mass concentration and processing conditions. Further, the addition of nanofillers will simultaneously alter the processing conditions of the final composites [3]. Carbon-based materials especially carbon nanotubes (CNT) have received increasing attentions as nanofillers due to their remarkable electrical and thermal conductivities (10^6 S/cm), high elastic modulus (1 TPa) and strength (10 GPa) [4]. Recently, a new class of high performance nanocomposites consisting of aligned CNT sheets, arrays and forests incorporated into various polymeric substrates have been studied for different applications in environmental remediation, and electrical and thermal management [5–9]. Multifunctional improvements in electrical, mechanical and thermal properties of these nanocomposites have been demonstrated by the formation of conductive CNT networks [5,6]. Sponge-like polymeric materials such as xerogel, foams, aerogel etc. offer the promise of developing lightweight nanocomposites with exceptional multifunctionalities and mechanical stability, as uniform dispersions of CNT in highly porous and interconnected network structures via template infiltration or impregnation become possible [2]. The key challenge of employing template infiltration is the development of high performance nanocomposites without compromising the mechanical integrity, flexibility and porosity of the template [10]. It has been reported that CNT-based composites tend to collapse under compression without exhibiting appreciable compressibility [11]. Accordingly, in-situ growth of an optimal amount of CNTs on a 3D macroporous structure is crucial for maintaining the mechanical stability and elastic modulus of polymer matrices while enhancing the electrical properties.

In this work, we have produced 3D, macroporous carbon foam structures reinforced with multi-walled CNTs using chemical vapor deposition (CVD). These lightweight CNT-reinforced polymeric nanocomposites have high adsorption capacity and are stable under compression and maintain full recovery to the original shape after a significant deformation at strains up to 90%. We have further evaluated these lightweight and flexible nanocomposites for both supercapacitors and hydrogen evolution reaction (HER) to establish the possibility of integrating energy conversion and storage into a single system. Furthermore, the development of flexible supercapacitor allows the combination of structural flexibility with high-power density of supercapacitors.

2. Characterization

2.1. Preparation of CNT nanocomposites

CNT-reinforced foams were prepared via a two-step process which consists of carbonization followed by a CVD. The first step carbonization of melamine-formaldehyde (MF) sodium bisulfite foams (Avocation Ltd, 25 mm thick) was carried out in an Ar atmosphere at 900 °C. After the carbonization, in-situ growth of CNT on the carbonized foams was achieved by using two different mass concentrations of precursors, 0.005 and 0.01 g ml^{-1} ferrocene-styrene (Sigma Aldrich) solution, which was introduced into the reaction tube at an injection rate of 0.8 ml/min, for a dwell time of 0.5–1 h. The resulting CNT-reinforced foams were named according to the mass concentration of the ferrocene-styrene solution and dwell time during the deposition. For example, CNT$_{0.005\_0.5h}$ refers to the foams prepared with 0.005 g ml^{-1} of ferrocene-styrene solution at the dwell time of 0.5 h. Reference carbon foam samples prepared by carbonization without CVD treatment were used for comparison against the foam nanocomposites.

2.2. Characterization and electrochemical testing

The morphological, structural and elemental characterization of the foams were conducted on a high-resolution transmission electron microscope (JEOL-2100 - HR-TEM) operated at 200 kV, Alpha FT-IR system with Platinum ATR setup (Bruker), scanning electron microscope (Hitachi S3200 N, Oxford instrument - SEM-EDS) operating at 20 kV, and X-Tek Benchtop 160Xi CT machine. X-ray diffraction patterns were recorded on a Bruker D8 Advance diffractometer (operated at 40 kV, 40 mA), with a Cu Kα radiation, at a step size and dwell time of 0.02° and 1 s respectively. Raman spectra were collected using a 532 nm laser excitation, utilizing a 50 × objective lens under a laser power of 6 mW. X-ray photoelectron spectra (XPS) were recorded using a VG ESCALab Mark II spectrometer with a non-monochromatic Al-anode X-ray source (1486.6 eV), operating at a 12 kV anode potential and a 20 mA filament emission current. Nitrogen adsorption/desorption was determined by Brunauer-Emmet-Teller (BET) measurements using a Quantachrome Autosorb-IQ surface area analyzer. Cyclic compression tests of the foams were carried out on a Lloyds EZ20 advanced universal mechanical testing system, using a 500 N detection cell at a loading rate of 8 mm/min. The elastic modulus was extrapolated from the linear region of the stress-strain curve. Electrochemical measurements were evaluated by cyclic voltammograms (CV), linear sweep voltammograms (LSV), impedance spectroscopy and galvanostatic charge-discharge tests on a CHI-760D potentiostat. The CHI-760D machine was coupled with a rotating disk electrode (RDE) system where the reference, counter and working electrodes were Ag/AgCl/KCl, platinum wire and glassy carbon electrode (GCE) covered with catalyst ink derived from the CNT-reinforced foams. The mass of active material was 0.212 mg cm^{-2}. The measurements were carried out in 0.5 M H_2SO_4 solution (Sigma Aldrich) at different potentials and scan rates varying from 0 to −0.8 V and 10–100 mV, respectively. The electrode was calibrated by a reversible hydrogen electrode (RHE) and acquired data were corrected for iR losses. The best performing foams were further subjected to stability test for 1000 cycles. Specific capacitance (C_{sp}) was derived from galvanostatic charge/discharge (GCD) using the equation: $C_{sp} = I/m$ ($\Delta V/\Delta t$) where I (A) is the discharge current, Δt (s) is the discharge time consumed in the potential window *of* ΔV (V) and m represents the mass of active material. The energy and power density were derived from galvanostatic charge/discharge curve using equations: $E = 0.5\ C_{sp}\ (\Delta V)^2$ and $P = E/\Delta t$ where E, P, ΔV and Δt represents energy density (Wh kg^{-1}), power density (kW kg^{-1}), potential window of discharge and discharge time, respectively.

3. Results and discussion

3.1. Structural and physicochemical properties

The carbon foams possess a 3D interconnected, macroporous framework with a density of 6.27 mg cm^{-3} (Fig. S1a). The TEM image and SAED pattern confirm that the carbon foam is made of amorphous carbon nanosheets, as shown in Fig. S1b.

After the carbonization and CVD treatment, multi-walled CNTs with diameters in the range of 40–150 nm are grown on the surface and truss of the carbon foam at the reaction temperature of 900 °C. The length of CNTs varies from a few to hundreds of μm depending on the precursor concentration. As shown in Fig. 1a–d, CNT morphology is also influenced by the precursor concentration.

At longer dwell time and higher precursor concentration, branched clumpy structures can be observed on the surface of the already grown, dense CNTs, due to the resulting Fe nanoparticles decomposed from ferrocene serving as nucleation spots for further CNT growth. This phenomenon agrees with the TEM results exhibited in Fig. 2 where CNT lumps and branches are observed. At maximum dwell time and precursor concentration, bamboo-like morphology, separated into several compartments by corrugated walls with encapsulated metal particle at the end of the sample and some compartments, can be observed for sample CNT$_{0.01\_1h}$ (Fig. 2g). The growth of these bamboo-like CNTs is linked to the Vapor-Liquid-Solid (VLS) mechanism, resulting in curvatures at the beginning of each compartment due to different bond
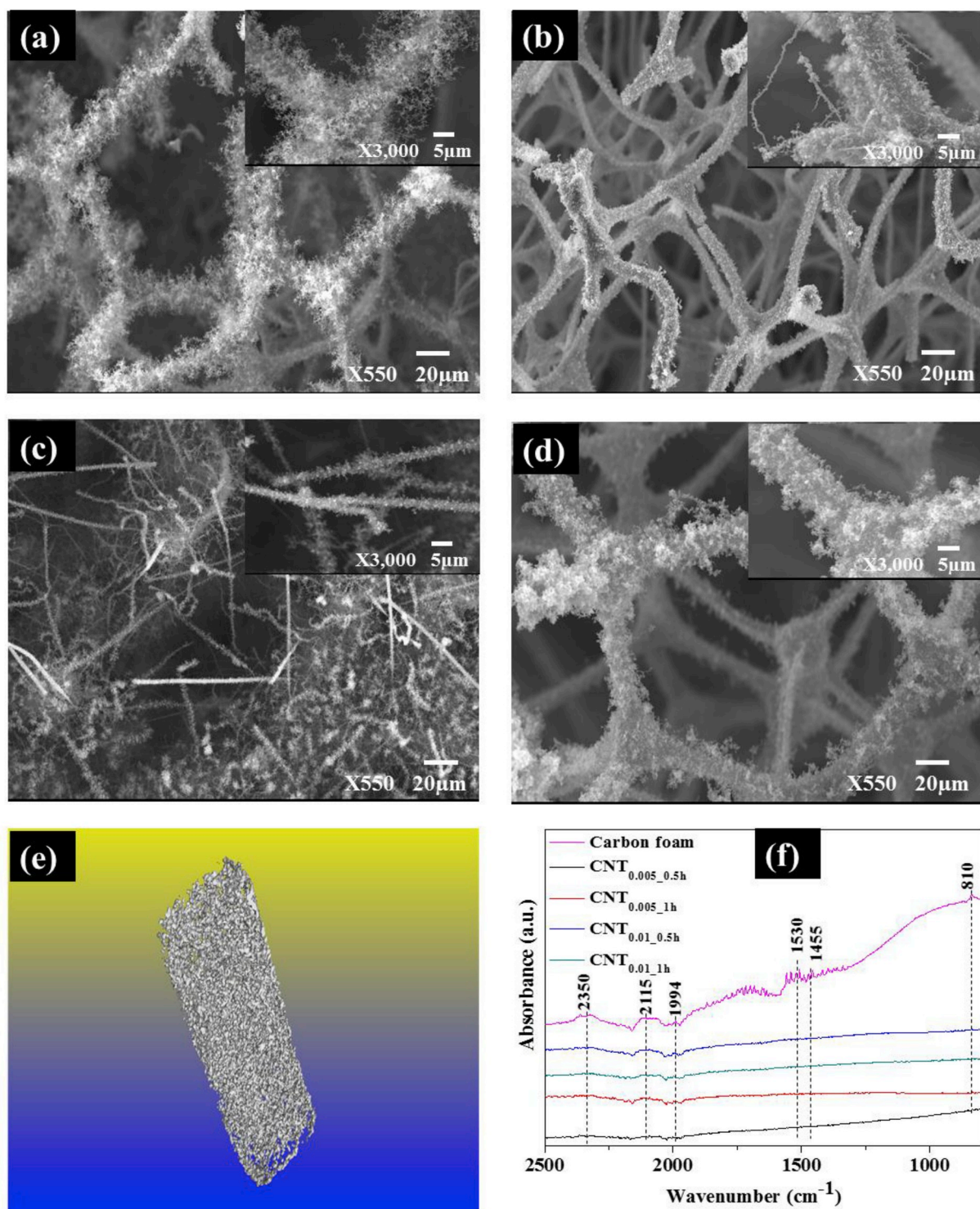
Fig. 1. Morphological and structural characteristics of the CNT-reinforced foams. (a) SEM micrograph of the $CNT_{0.005\_0.5h}$ foam; (b) SEM micrograph of the $CNT_{0.005\_1h}$ foam; (c) SEM micrograph of the $CNT_{0.01\_0.5h}$ foam; (d) SEM micrograph of the $CNT_{0.01\_1h}$ foam; (e) Micro-CT image of $CNT_{0.01\_1h}$ foam; and (f) ATR-FTIR spectra of the CNT-reinforced foams synthesized at different mass concentrations of precursors and dwell time.

lengths of C–C and C–N [12,13]. C and N elements originate from the carbonization of melamine precursor that is nitrogen-rich. The interlayer spaces of the CNT-reinforced foams are in the range of 0.34–0.36 nm, which corresponds to the (002) plane of graphitic carbon [12].

The densities of CNT-reinforced foams increased to 8–10.2 mg cm^{-3} with increasing precursor concentrations. According to the elemental analyses, the CNT-reinforced foams contain mainly C and N (from the melamine foam), with residual Fe originating from ferrocene. As shown in Fig. 1e, the CNT reinforced foams still maintain their hierarchical porous structure with concave-shaped fibers formed after the CVD process. The ATR-FTIR spectra of the foams are presented in Fig. 1f. Peaks at 810 and 1455 cm^{-1} are observed for the carbon foam only, which can be linked to the vibration modes of s-triazine ring of the melamine precursor. The peak at 1530 cm^{-1} is attributed to the C═N stretching vibration of s-triazine ring [14]. The CNT reinforced foams
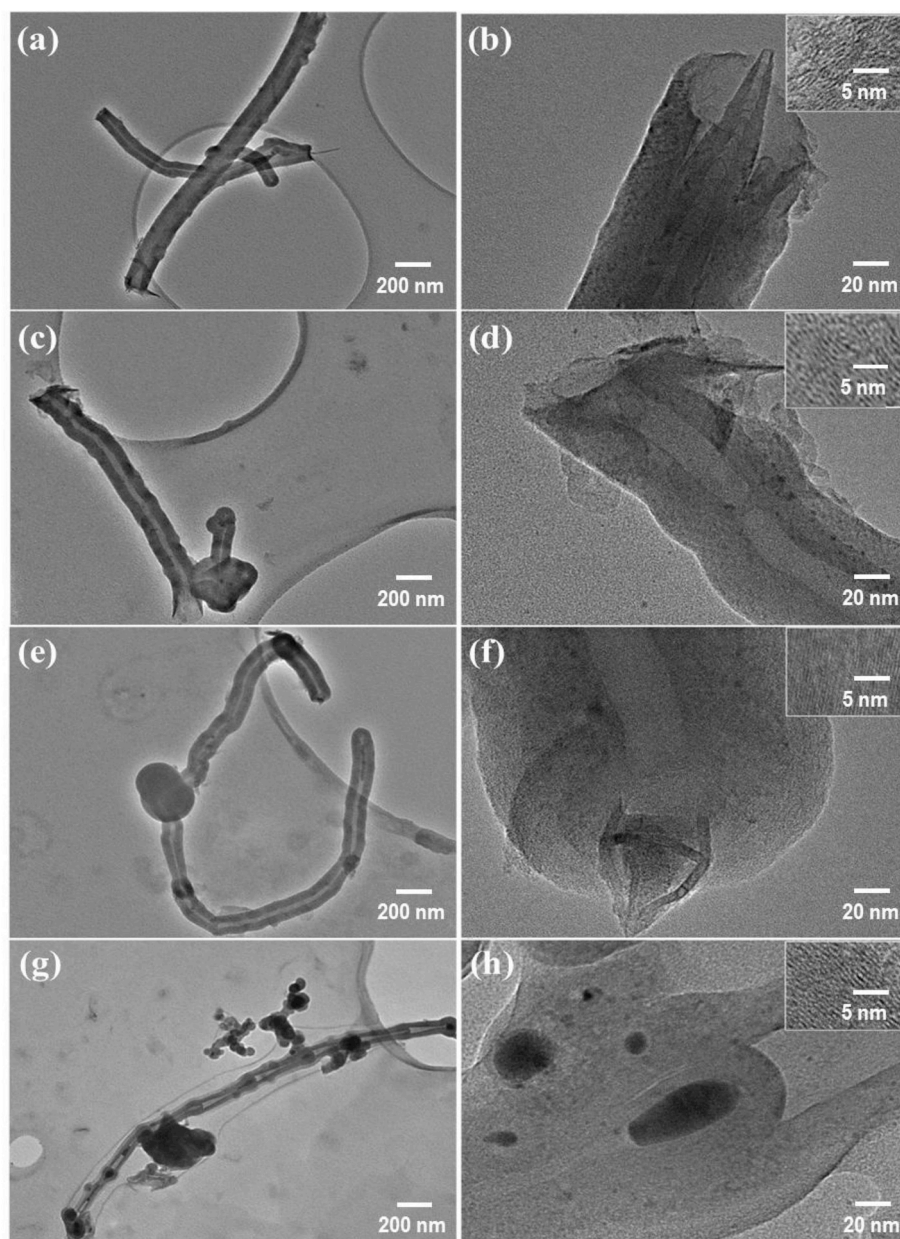
Fig. 2. TEM micrographs of the CNT reinforced foams. (a–b) $CNT_{0.005\_0.5h}$; (c–d) $CNT_{0.005\_1h}$; (e–f) $CNT_{0.01\_0.5h}$ and (g–h) $CNT_{0.01\_1h.}$ The inset shows the corresponding lattice fringe of the carbon structures.

have absorption peaks at the 2115 and 2350 cm^{-1} region, which is due to the C≡N stretching [15,16]. The 1994 cm^{-1} peak is linked to bridge carbonyl groups [17]. In the XRD results, as shown in Fig. S2, the foams possess broad diffraction peaks, owing to the low degree of graphitization. The X-ray diffraction peaks at 13.1° can be assigned to (100) plane of amorphous carbon nitride (g-C_3N_4) [18,19], whilst the 29.3° peak originates from the melamine precursor. As indicated by the BET results, the walls of the carbon foam are mainly composed of mesoporous carbon having pore size greater than 2.8 nm, and carbon foams possess a specific surface area of 159 $m^2 g^{-1}$ (Fig. S3). Compared with the plain carbon foam, CNT-reinforced foams exhibit higher specific surface area, ranging from 202 to 524 $m^2 g^{-1}$ with the $CNT_{0.005\_1h}$ foam having the maximum value. Improved surface areas resulting from the direct in-situ growth of CNTs and porous structure offer the possibility of efficient electron and ion transfer required for enhanced electrochemical performance.

Fig. 3 shows the Raman features of the foams. All foams possess

Raman bands at frequencies of 1347.6–1356 cm^{-1} which represents the D peak in disorder-induced carbon with defects. The bands at 1579.6–1588.9 cm^{-1} can be assigned to the in-plane stretching vibration mode of the G band of graphitic carbon. The intensity ratio of D to G peak (I_D/I_G) of the CNT-reinforced foams is within the range of 0.89–1.24. The $CNT_{0.01\_1h}$ foam has the lowest I_D/I_G ratio of 0.89 which implies that it has fewer defects compared to other foams [20]. Other main peaks at ~2680 cm^{-1} corresponds to the overtone of the D band and high energy second order process in graphene. The intensity ratios of G to 2D peak (I_G/I_{2D}) can be used to estimate the number of graphene layer. The 2D peak has been labelled as G' in this manuscript and the I_G/I_{2D} values vary from 1.2 to 1.5 which implies that graphene consists of at least three layers [21,22].

XPS was used to characterise the chemical bonds of carbon and CNT-reinforced foams (Fig. S4). Although no Fe peaks were observed for the CNT-reinforced foams by the XPS, elemental analyses by SEM-EDS confirms that CNT-reinforced foams are primarily composed of C and
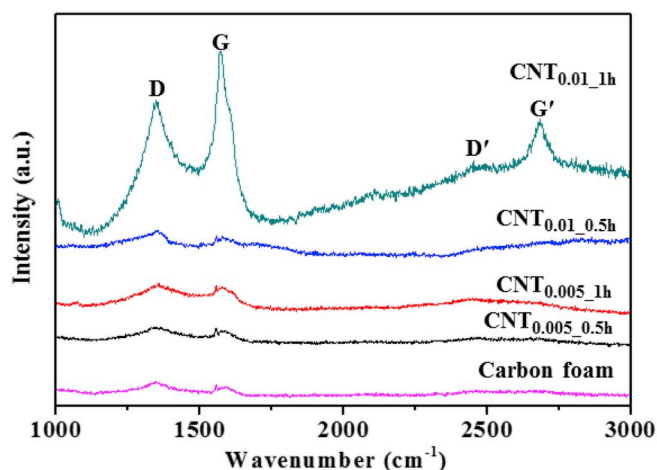
Fig. 3. Raman spectra of carbon and CNT-reinforced foams.

N with Fe present in small concentrations up to 4.38%. All samples possess several characteristic peaks for C 1s states. Peaks due to carbon – carbon interaction that are present at ~284.4 and 285 eV belong to the sp^2 hybridized graphite like carbon (C=C) and the sp^3 hybridized diamond-like carbon (C–C) bonds where carbon bonds with nitrogen as C–N, respectively [23,24]. The intensity of the C–C sp^2 bonds decrease with increasing the precursor concentration and dwell time while intensity of C–C sp^3 bonds remains unaffected. Existence of π-π^* shakeup features was also observed for all foams apart from the $CNT_{0.005\_1h}$ foam. For carbon – oxygen interaction, peaks at higher binding energies in the range of 286.8–288.5 eV and 289.1–290.7 eV represents C–O and C=O bonds, respectively [23,24]. Decomposition of oxygen containing moieties in samples with increasing precursor concentration and dwell time occurred after thermal treatment since the peak intensity decreased [23]. The high-resolution spectra of N1s can be further deconvoluted into four peaks based on their binding energies: pyridinic-N (398 eV), pyrrolic-N (399.9 eV), quaternary-N (401.2 eV), and pyridine-N-oxide (403.6 eV). The majority of N in the foams appears to exist as pyridinic-N and pyrrolic-N.

The effect of CNT loading on the mechanical properties of carbon and CNT-reinforced foams were investigated, and the results are shown in Figs. 4 and S5. The compressive stress as a function of the strain at 90% was evaluated for different cycles. All CNT-reinforced foams display an elastic linear region due to bending of the CNT-reinforced foam, followed by a plateau region and densification of the foam with increased stress, similar to other compressible foams [25].

The CNT-reinforced foams show an excellent mechanical stability at large compressive strains of 90%, with all unloading curves having similar trend lines and returning to their original position, due to the foam truss forming an interlinked, elastic 3D network. Compared to pristine carbon foam (Fig. S5), CNT-reinforced foams exhibit slight reduction in compressive properties with increasing CNT concentration. The compressive strength of $CNT_{0.01\_1h}$ foam was reduced by 29% compared with the $CNT_{0.005\_1h}$ foam that exhibited the maximum compressive strength of 103 KPa. The elastic modulus of $CNT_{0.005\_1h}$ foam also increases by 24% compared with that of the $CNT_{0.01\_1h}$ foam. After 100 cycles at 90% strain, $CNT_{0.01\_1h}$ foam still maintains its mechanical stability, and its unloading curve returns to its original position, however, its compressive stress drops by 70%. This indicates the non-
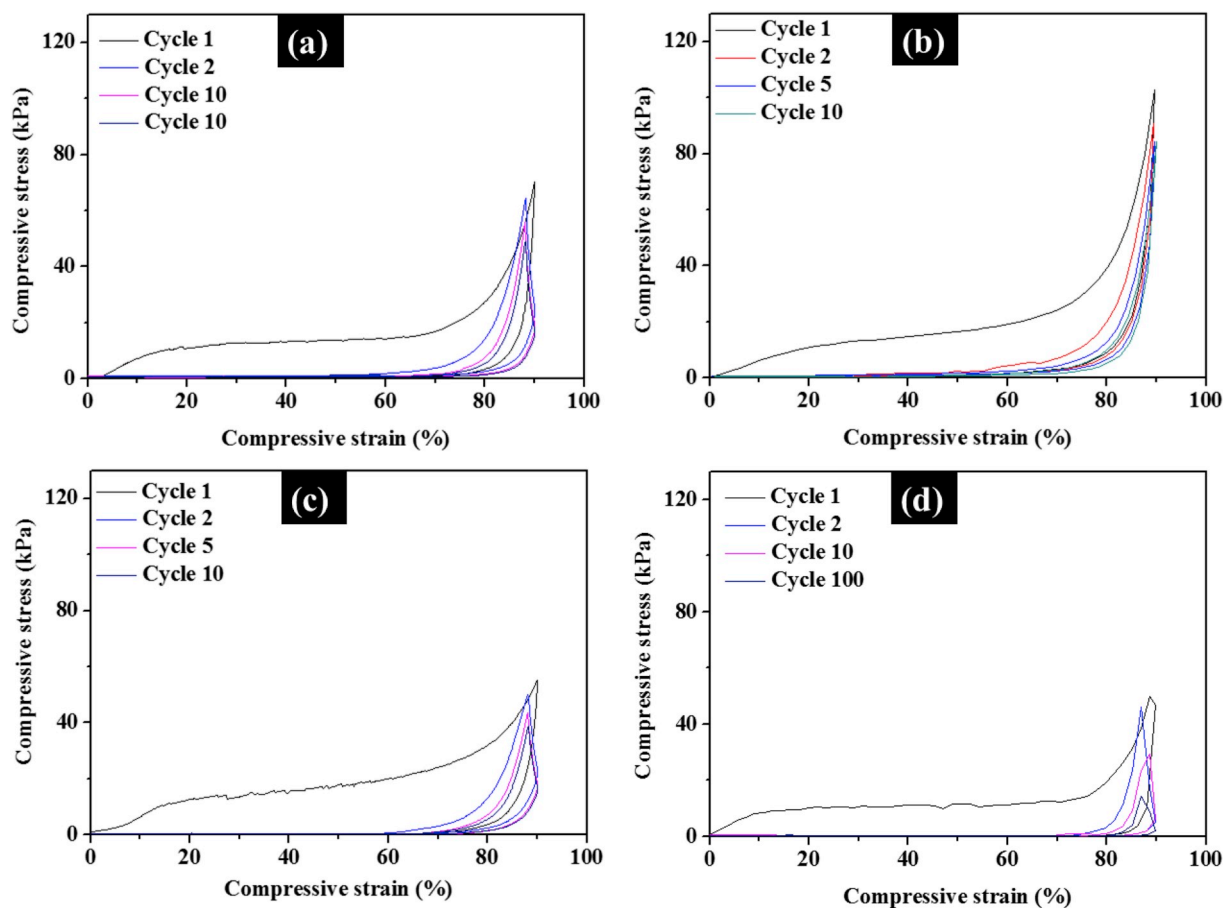

Fig. 4. Cyclic compressive behavior of (a) $CNT_{0.005\_0.5h}$; (b) $CNT_{0.005\_1h}$; (c) $CNT_{0.01\_0.5h}$ foam; and (d) $CNT_{0.01\_1h}$ with a 90% strain, tested at a loading rate of 8 mm/min.

recoverable feature of the foam to its original size due to van der Waals's adhesion between CNTs under high compressive strains [3]. Linear shrinkage of the foam by 48% can be observed due to the structural densification and reorientation of its reinforcing CNT fibers rather than from the collapse of the entire foam network. Comparatively, this superb load bearing capacity and mechanical stability of $CNT_{0.01\_1h}$ foam at 15 KPa obtained at a load of 50 N and at a strain of 90% cannot be observed in most CNT sponges reported. For example, a CNT sponge was reported to achieve excellent stability at ~14 KPa for 1000 cycles at a load of merely 0.05 N and under a similar strain of 90% [26]. This phenomenon is due to the CNT reinforcement grown on the 3D truss network of the foam, such that the compressive force applied on each foam truss is transferred to the elastic foam bulk to attain complete recovery even after large deformation.

3.2. Electrochemical properties

The electrochemical performance of the flexible CNT-reinforced foams towards hydrogen evolution (HER) and energy storage (supercapacitor) was evaluated in 0.5 M H_2SO_4 solution. The HER linear sweep voltammetry for commercial benchmark catalyst, 20 wt% Pt/C and foam-based samples is presented in Fig. 5a. Typical polarization curve for the foam-based samples demonstrates that $CNT_{0.005\_1h}$ foam presents a low onset overpotential of ~0.1 V versus RHE for initiating HER evolution. Pristine carbon foam exhibits HER activity with the highest overpotential, however, the electrochemical performance in terms of current density is limited, due to its low electrical conductivity. Conversely, at the reference value of 10 mA cm^{-2}, the CNT-reinforced

foams demonstrated an improved HER activity. This indicates the contributing role of Fe and N species contained in the CNT-reinforced foam framework in providing active sites to catalyse HER reaction. $CNT_{0.005\_1h}$ foam exhibits the earliest onset of catalytic current and maximum HER current density compared with other samples. An overpotential of 240 mV vs. RHE was required by $CNT_{0.005\_1h}$ foam to reach a current density of 10 mA/cm^2. The difference in HER performance might be linked to different morphologies and CNT content in the foams. The HER activity of the present foams is higher than [27], or comparable with, that of other CNT- and metal-coated foam-based structures reported [28,29]. Fig. 5b shows the Tafel slopes of the foam-based samples. The linear regions of Tafel plots were fit to Tafel equation ($\eta = b \log j + a$ where b and j is the Tafel slope and current density, respectively). The lowest Tafel slope of 56 mV was obtained for the $CNT_{0.005\_1h}$ foam which is linked to an increased HER activity. Based on this Tafel slope value, it can be suggested that the mechanism of the HER process of $CNT_{0.005\_1h}$ foam involves both Volmer and Heyrovsky reactions where electrochemical desorption (i.e. conversion of protons into adsorbed hydrogen atoms) and formation of hydrogen molecules occurred, respectively.

The mechanism for HER activity on the CNT-reinforced foams was further investigated via electrochemical impedance spectroscopy (EIS), and the Nyquist plots of the EIS responses are shown in Fig. 5c. The charge transfer resistance (R_{CT}) decreases remarkably from 388 Ω for $CNT_{0.01\_1h}$ to 18 Ω for strongly coupled $CNT_{0.005\_1h}$ foam. In contrast, the pristine carbon foam exhibits an impeded R_{CT} as high as ~610 Ω (Fig. 5c). The results confirm that the growth of CNT on the concave shaped trusses has influenced the electrochemical activity and charge
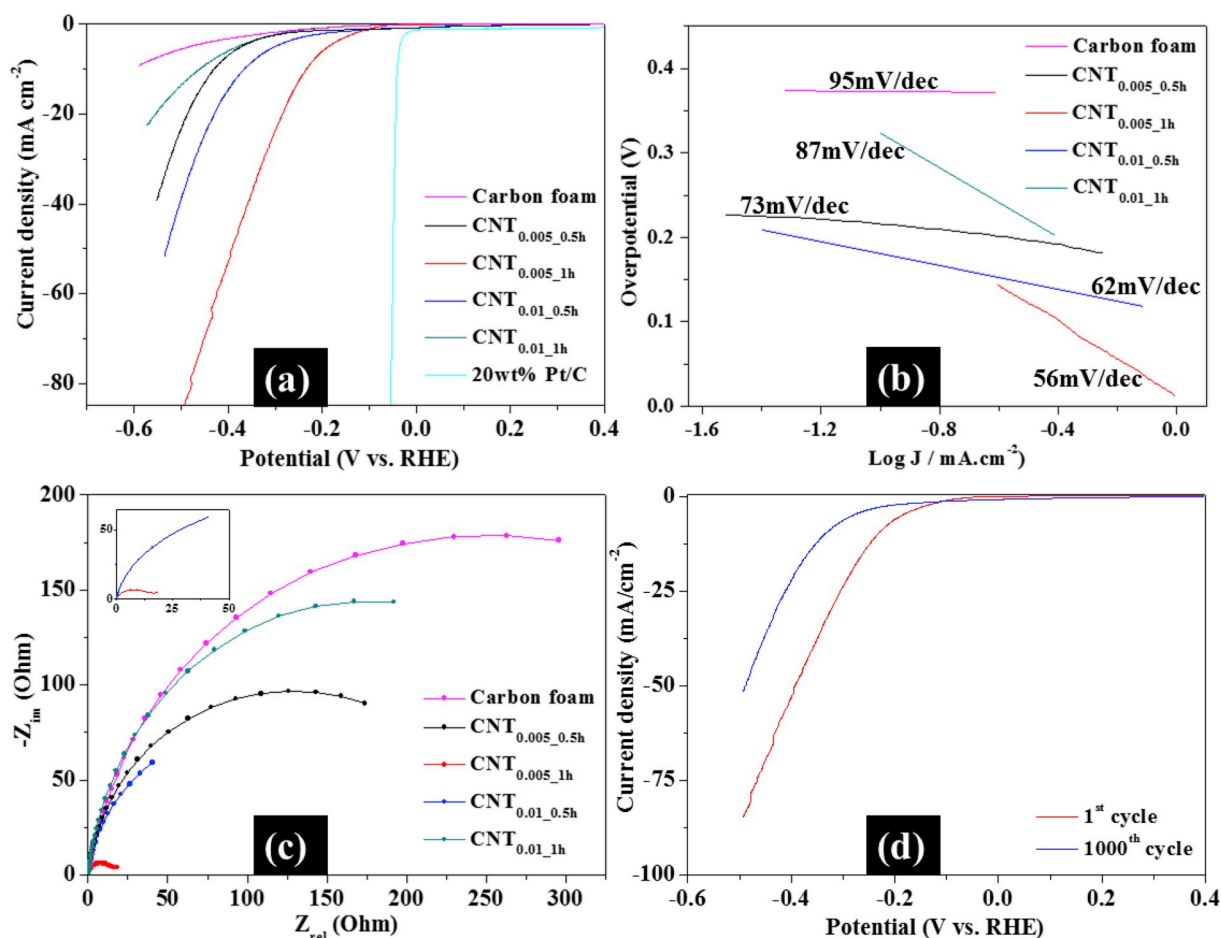

Fig. 5. (a) Polarization curves of 20 wt% Pt/C, carbon and CNT-reinforced foams in 0.5 M H_2SO_4, (b) Tafel plots, (c) Nyquist plots at 250 mV overpotential, and (d) HER polarization curve of $CNT_{0.005\_1h}$ before and after 1000 cycles of CV in 0.5 M H_2SO_4.

transfer behavior of the carbon foams. A comparison of $CNT_{0.005\_1h}$ foam with the other foam-based samples indicates that $CNT_{0.005\_1h}$ possesses a better interfacial attachment with carbon nanosheets, thereby resulting in a lower R_{CT} and shorter electron transport to active sites. The electrochemical stability of the best performing foam was evaluated for 1000 cycles from 0.4 to -0.6 V vs. RHE (Fig. 5d). The $CNT_{0.005\_1h}$ foam shows almost a 38% loss of its HER activity after 1000 cycles. The loss could be attributed to the weak interaction between CNT and the carbon foam.

The performance of the flexible CNT-reinforced foams was evaluated for energy storage applications with galvanostatic charge-discharge measurements. Figs. 6 and S5 show the CV curves of carbon and CNT-reinforced foams recorded at scan rates of 10–100 mV/s within a voltage window of 0.2–0.8 V in 0.5 M H_2SO_4.

The symmetric and rectangular shape of CV curves is maintained at high scan rates which indicates good capacitive behavior. The specific capacitance was calculated from the galvanostatic charge-discharge measurements carried out at a charge/discharge current density range of 2–6.7 A g^{-1}, and the results are shown in Figs. 6 and S6. The charging curves are symmetrical to the resulting discharging curves, and the CNT-reinforced foams exhibit a specific capacitance as high as 776 F g^{-1} at a low current density of 2 A g^{-1}. The improved specific capacitance can be linked to the high specific surface areas measured by nitrogen adsorption. The $CNT_{0.005\_1h}$ foam exhibits the maximum surface area of 524 m^2 g^{-1} compared with the pristine carbon foam and other CNT-reinforced foams, so that its specific capacitance is much higher than that of the pristine carbon foams. As shown in Fig. 6c, the $CNT_{0.005\_1h}$

foam not only attained a high specific capacitance but maintained it at higher current densities, against other foams investigated. A capacitance of 607 F g^{-1} was retained when the current density was increased to 6.7 A g^{-1}, implying that the CNT-reinforced foam can retain 77.9% of its initial capacitance when the current density is 3.4 times higher than its initial value.

At higher current density, the decrease in specific capacitance is due to limited ion diffusion and increased resistance from the high kinetic energy of ions. The stability of $CNT_{0.005\_1h}$ foam was monitored by evaluating the specific capacitance after 1000 CV cycles, and it retained 96% of its initial capacitance at a constant current density of 2 A g^{-1} (Fig. 5d). We believe that the presence of Fe, C and N species anchored on the three-dimensional CNT-reinforced foams contributed to the excellent capacitive performance, by providing enhanced reaction kinetics and reduced diffusion path for the ion-pore interaction. As shown in Table S1, the specific capacitive performance of present foams is comparable to other similar carbon-based nanocomposites reported in literature. Fig. 7 shows the Ragone plot of the $CNT_{0.005\_1h}$ foam. An increase in current density from 2 to 6.67 A g^{-1} results in the energy density reaching a minimum at 84.3 Wh kg^{-1}. Conversely, the $CNT_{0.005\_1h}$ foam exhibits a power density of 3.33 kW kg^{-1} at a current density of 6.67 A g^{-1}. Thus, the optimal sample, $CNT_{0.005\_1h}$ foam possesses energy and power density of 108 Wh kg^{-1} and 1 kW kg^{-1}, respectively, which is slightly higher compared to other carbon-based hybrid nanocomposites (Table S1).

Overall, the $CNT_{0.005\_1h}$ foam demonstrates the best electrochemical performance, especially for HER, due to its high specific surface area,
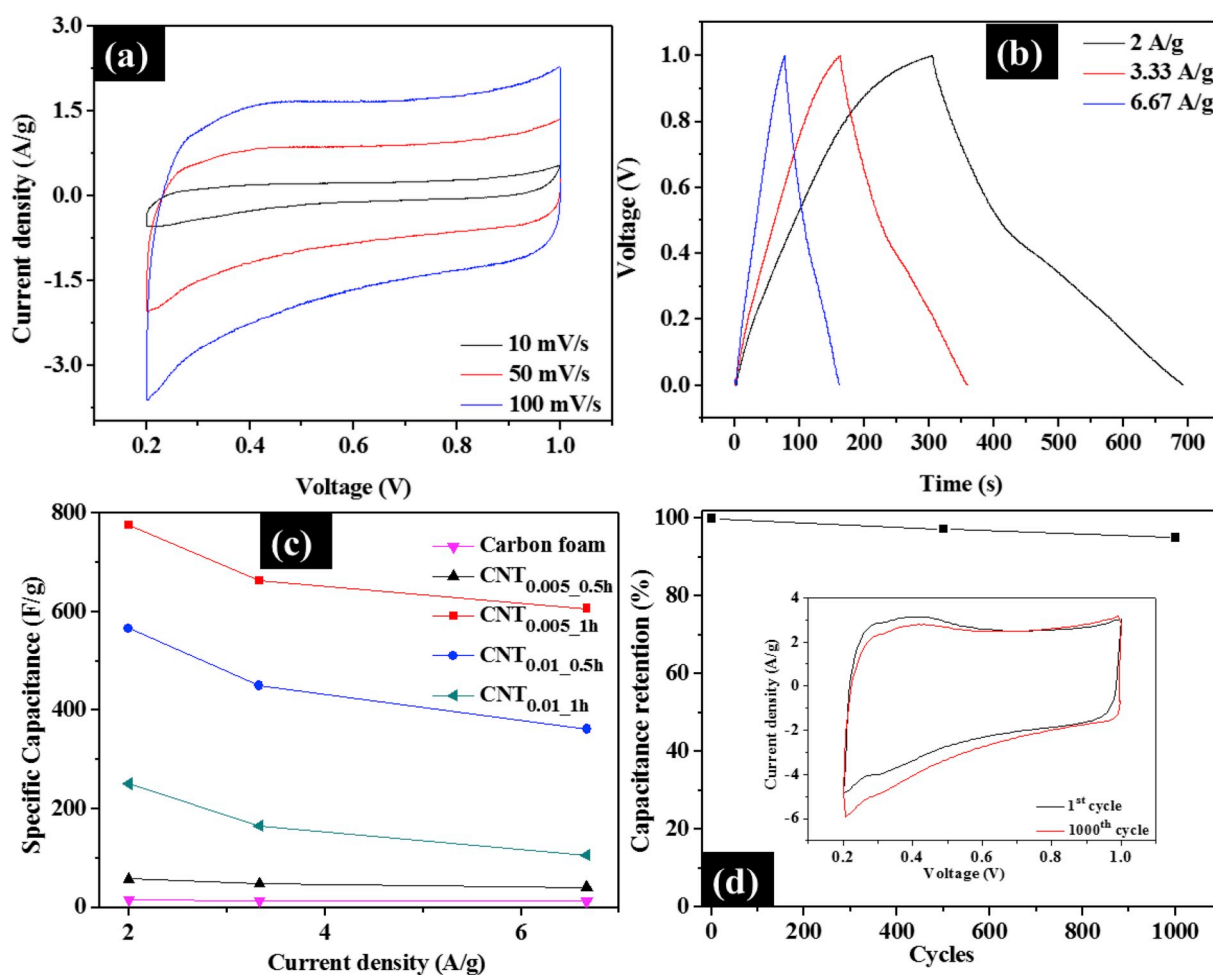

Fig. 6. (a) CV curves of $CNT_{0.005\_1h}$ at scan rates of 10–100 mV/s, (b) charge-discharge curves of $CNT_{0.005\_1h}$ at different current densities, (c) specific capacitance of the CNT-reinforced foams as a function of current density, in 0.5 M H_2SO_4, and (d) cycling performance of the $CNT_{0.005\_1h}$ foam at 1st and 1000th cycles, at 2 A g^{-1}.
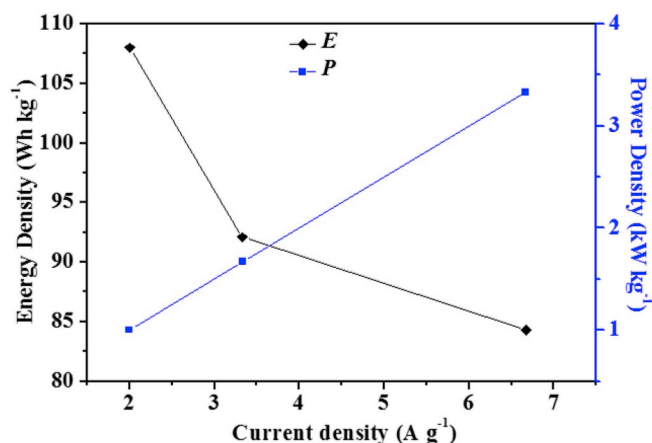
Fig. 7. Variation of energy and power densities of $CNT_{0.005\_1h}$ at different current densities.

catalytic sites linked to Fe and N species and the increased conductivity and shortened ion transport path derived from the multi-walled CNTs in the flexible 3D network. The hierarchical porous conductive network of the CNT-reinforced foams will also facilitate exposure of more catalytic sites and enhance the ion/electron and mass transport pathways via increased ion-pore interaction while maintaining its structural integrity and cycling stability over a wide voltage window.

4. Conclusions

In this work, multi-walled CNTs were grown on the trusses of interconnected, macroscopic carbon foams using a simple method, to attain multifunctional nanocomposites that possess combined properties of the superb structural flexibility, high strength to weight ratio and mechanical stability. The CNT-reinforced nanocomposites are suitable for energy conversion and storage applications and extend the existing superb mechanical and structural features to electrochemical arena by benefiting the ion transport and electric conductivity. These nano-composites exhibit excellent electrochemical performances with an overpotential of 240 mV to reach a current density of $10\,mA\,cm^{-2}$ for HER. In addition to the high specific capacitance, the composite foam electrode also shows excellent stability after 1000 cycles. The results demonstrate that the physicochemical properties of multifunctional 3D composite foams developed from the simultaneous carbonization and chemical treatment of polymeric templates can be further exploited for energy and environmental related applications.

Declaration of competing interest

The authors declare that they have no known competing financial interests or personal relationships that could have appeared to influence the work reported in this paper.

Acknowledgments

Appendix A. Supplementary data

Supplementary data to this article can be found online at https://doi.org/10.1016/j.jpowsour.2019.227277.

References

[1] L. Chen, D. Rende, L.S. Schadler, R. Ozisik, "Polymer nanocomposite foams", J. Mater. Chem. A (2013) 3837–3850, https://doi.org/10.1039/C2TA00086E 1.

[2] B. Hao, P.C. Ma, "Chapter 3 - carbon nanotubes for defect monitoring in fiber-reinforced polymer composites A2 - peng, huisheng", in: Q. Li, T. Chen (Eds.), Industrial Applications of Carbon Nanotubes, Elsevier, Boston, 2017, pp. 71–99.

[3] E.-C. Cho, C.-W. Chang-Jian, Y.-S. Hsiao, K.-C. Lee, J.-H. Huang, "Three-dimensional carbon nanotube based polymer composites for thermal management", Compos. Appl. Sci. Manuf. 90 (2016) 678–686.

[4] M.Q. Jian, H.H. Xie, K.L. Xia, Y.Y. Zhang, "Chapter 15 - challenge and opportunities of carbon nanotubes A2 - peng, huisheng", in: Q. Li, T. Chen (Eds.), Industrial Applications of Carbon Nanotubes, Elsevier, Boston, 2017, pp. 433–476.

[5] X. Gui, et al., "Carbon nanotube sponges", Adv. Mater. 22 (2010) 617–621.

[6] Z. Yingying, et al., "Polymer-embedded carbon nanotube ribbons for stretchable conductors", Adv. Mater. 22 (2010) 3027–3031.

[7] Y. Hu, W. Chen, L. Lu, J. Liu, C. Chang, "Electromechanical actuation with controllable motion based on a single-walled carbon nanotube and natural biopolymer composite", ACS Nano 4 (2010) 3498–3502.

[8] I. Hjorth, M. Nord, M. Rønning, J. Yang, D. Chen, "Electrochemical reduction of CO2 to synthesis gas on CNT supported CuxZn1-x O catalysts", Catal. Today (2019). https://doi.org/10.1016/j.cattod.2019.02.045.

[9] C. Ji, et al., "Thermal conductivity enhancement of CNT/MoS2/graphene−epoxy nanocomposites based on structural synergistic effects and interpenetrating network", Compos. B Eng. 163 (2019) 363–370.

[10] M. Inagaki, F. Kang, M. Toyoda, H. Konno, Advanced Materials Science and Engineering of Carbon, Butterworth-Heinemann, 2013.

[11] X. Gui, et al., "Soft, highly conductive nanotube sponges and composites with controlled compressibility", ACS Nano 4 (2010) 2320–2326.

[12] X. Wu, Y. Tao, Y. Lu, L. Dong, Z. Hu, "High-pressure pyrolysis of melamine route to nitrogen-doped conical hollow and bamboo-like carbon nanotubes", Diam. Relat. Mater. 15 (2006) 164–170.

[13] B. Padya, D. Kalita, P.K. Jain, G. Padmanabham, M. Ravi, K.S. Bhat, "Self-organized growth of bamboo-like carbon nanotube arrays for field emission properties", Appl. Nanosci., journal article 2 (2012) 253–259.

[14] D.J. Merline, S. Vukusic, A.A. Abdala, "Melamine formaldehyde: curing studies and reaction mechanism", Polym J, Original Article 45 (2012) 413.

[15] A.C. Ferrari, S.E. Rodil, J. Robertson, "Interpretation of infrared and Raman spectra of amorphous carbon nitrides", Phys Rev B 67 (2003) 155306.

[16] A. Stolz, et al., "Melamine-derived carbon sponges for oil-water separation", Carbon 107 (2016) 198–208.

[17] G. Raj, A. Bhagi, V. Jain, Group Theory and Symmetry in Chemistry, Krishna Prakashan Media Ltd, 2010.

[18] Z. Chen, W. Ren, L. Gao, B. Liu, S. Pei, H.-M. Cheng, "Three-dimensional flexible and conductive interconnected graphene networks grown by chemical vapour deposition", Nat. Mater. 10 (2011) 424.

[19] M.L. Scheepers, R.J. Meier, L. Markwort, J.M. Gelan, D.J. Vanderzande, B.J. Kip, "Determination of free melamine content in melamine-formaldehyde resins by Raman spectroscopy", Vib. Spectrosc. 9 (1995) 139–146.

[20] R. Muzyka, S. Drewniak, T. Pustelny, M. Chrubasik, G. Gryglewicz, "Characterization of graphite oxide and reduced graphene oxide obtained from different graphite precursors and oxidized by different methods using Raman spectroscopy", Materials 11 (2018) 1050.

[21] A. Reina, et al., "Large area, few-layer graphene films on arbitrary substrates by chemical vapor deposition", Nano Lett. 9 (2009) 30–35.

[22] Z. Li, et al., "Graphene thickness control via gas-phase dynamics in chemical vapor deposition", J. Phys. Chem. C 116 (2012) 10557–10562.

[23] B.-J. Kim, J.-P. Kim, J.-S. Park, "Effects of Al interlayer coating and thermal treatment on electron emission characteristics of carbon nanotubes deposited by electrophoretic method", Nanoscale Res. Lett. 9 (2014) 236.

[24] S. Kim, J. Kim, J. Lim, H. Lee, Y. Jun, D. Kim, "A coaxial structure of multiwall carbon nanotubes on vertically aligned Si nanorods and its intrinsic characteristics", J. Mater. Chem. C (2014) 6985–6990, https://doi.org/10.1039/C4TC01251H 2.

[25] H. Liu, et al., "Lightweight conductive graphene/thermoplastic polyurethane foams with ultrahigh compressibility for piezoresistive sensing", J. Mater. Chem. C (2017) 73–83, https://doi.org/10.1039/C6TC03713E 5.

[26] Z. Dai, et al., "Three-dimensional sponges with super mechanical stability: harnessing true elasticity of individual carbon nanotubes in macroscopic architectures", Sci. Rep. (2016) 18930. Article 6.

[27] D.J. Li, et al., "Molybdenum sulfide/N-doped CNT forest hybrid catalysts for high-performance hydrogen evolution reaction", Nano Lett. 14 (2014) 1228–1233.

[28] S.-K. Park, D.Y. Chung, D. Ko, Y.-E. Sung, Y. Piao, "Three-dimensional carbon foam/N-doped graphene@MoS2 hybrid nanostructures as effective electrocatalysts for the hydrogen evolution reaction", J. Mater. Chem. A (2016) 12720–12725, https://doi.org/10.1039/C6TA03458F 4.

[29] J. Cao, J. Zhou, Y. Zhang, X. Liu, "A clean and facile synthesis strategy of MoS2 nanosheets grown on multi-wall CNTs for enhanced hydrogen evolution reaction performance", Sci. Rep. 7 (2017) 8825.